Supplementary information for

"Hyperbolic Plasmons Propagate through a Nodal Metal"

Yinming Shao[1], Aaron J. Sternbach[1], Brian S. Y. Kim[2], Andrey A. Rikhter[3], Xinyi Xu[2], Umberto De Giovannini[4], Ran Jing[1], Sang Hoon Chae[2], Zhiyuan Sun[1], Yanglin Zhu[5], Zhiqiang Mao[5], J. Hone[2], Raquel Queiroz[1], A. J. Millis[1,6], P. James Schuck[2], A. Rubio[4,6], M. M. Fogler[3], D. N. Basov[1]

[1]Department of Physics, Columbia University, New York, NY, 10027, USA

[2]Department of Mechanical Engineering, Columbia University, New York, NY, 10027, USA

[3]Department of Physics, University of California, San Diego, La Jolla, CA, 92093, USA

[4]Max Planck Institute for the Structure and Dynamics of Matter, Center for Free Electron Laser Science, Hamburg 22761, Germany

[5]Department of Physics, Pennsylvania State University, University Park, PA, 16802, USA
[6]Center for Computational Quantum Physics (CCQ), Flatiron Institute, New York, NY, 10010, USA

Contents

Section S1: Dielectric function and optical conductivity of ZrSiS and ZrSiSe

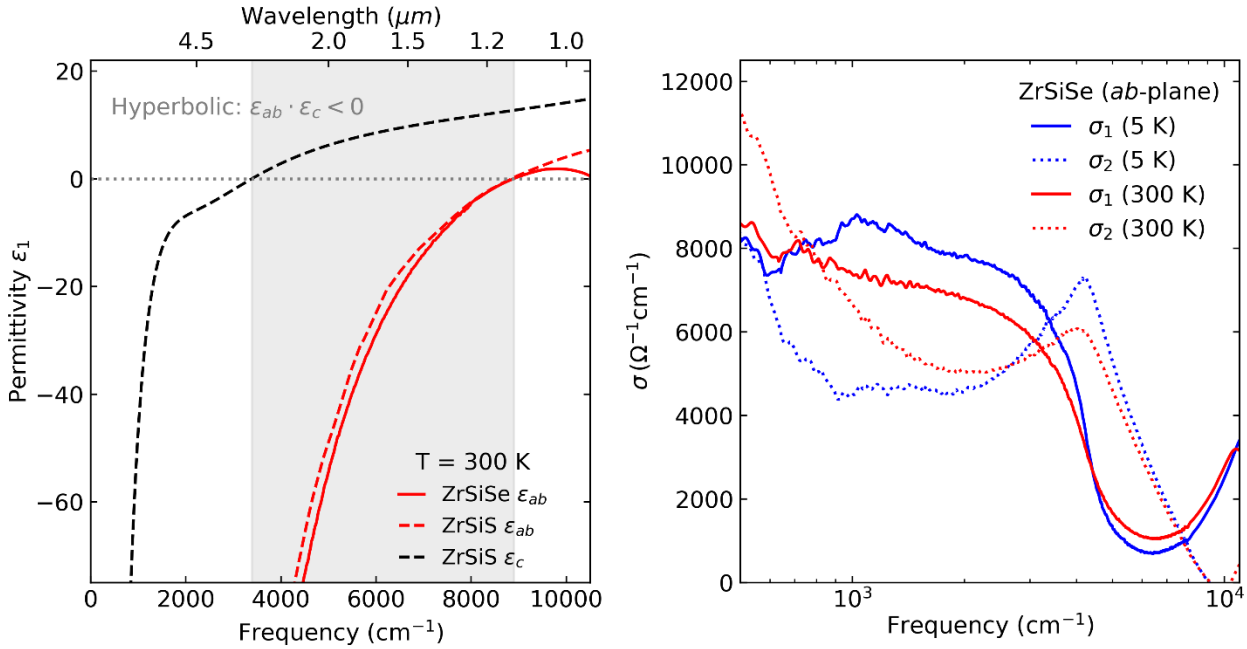

Figure S1. (Left) Real part of the dielectric function of ZrSiS (dashed lines) and ZrSiSe (solid line). The gray-shaded region indicates the frequency range where ZrSiS is hyperbolic. (Right) *ab*-plane optical conductivities of ZrSiSe at 300 K and 5 K. Solid and dotted lines represent the real and imaginary parts of $\sigma(\omega) = \sigma_1 + i\sigma_2$, respectively.

The *ab*-plane complex optical conductivity ($\sigma(\omega) = \sigma_1 + i\sigma_2$) of bulk ZrSiSe is obtained using broadband reflectance spectra combined with spectroscopic ellipsometry[1]. To study the hyperbolicity the *c*-axis dielectric response is also important. While an optically flat *ac*-surface is not attainable in ZrSiSe, measurements on the large and flat *ac*-surface of a closely related ZrSiS compound indeed reveal a much lower plasma frequency along the *c*-axis (Fig. S1, black dashed line), consistent with recent report[2]. Given the similar *ab*-plane optical responses of ZrSiS[3] and ZrSiSe[1], their hyperbolic frequency regions are presumed to be closely matched as well.

As mentioned in the main text, the unique nodal-line structure of ZrSiSe offers an effective approach to reducing the electronic loss associated with interband optical transitions. More specifically, in Fig. S2a, numerous “nodal-points" exist (red-shaded plane) for two-dimensional (2D) cuts away from the vertical nodal-lines (gray-shaded plane). For flat nodal-lines (Fig. S2b), the real optical conductivity follows a frequency-independent power law $\sigma_1 \sim$const. across a large frequency spectrum[1,3–5], resulting from its linear-in-frequency joint density of states (JDOS). However, the 2D planes away from vertical nodal-lines support van Hove singularities between the nodal-points, as shown schematically in Fig. S2c. The van Hove singularities then imply that the JDOS will stop increasing above the van Hove energy Δ' and the corresponding σ_1 will decrease[1,5], as illustrated in Fig. S2d.

Although van Hove singularities appear in many electronic systems (e.g., Weyl semimetals), the impact on the optical conductivity of 3D systems rarely leads to a minimum, due to the large

JDOS. For a pair of Weyl nodes shown in Fig. S2e, the JDOS scales with frequency as ω^2 and correspondingly, $\sigma_1(\omega) \propto \mathrm{JDOS}/\omega = \omega$. As a result, the van Hove singularity only changes the slope of the linear scaling of σ_1 in a Weyl semimetal[6,7].

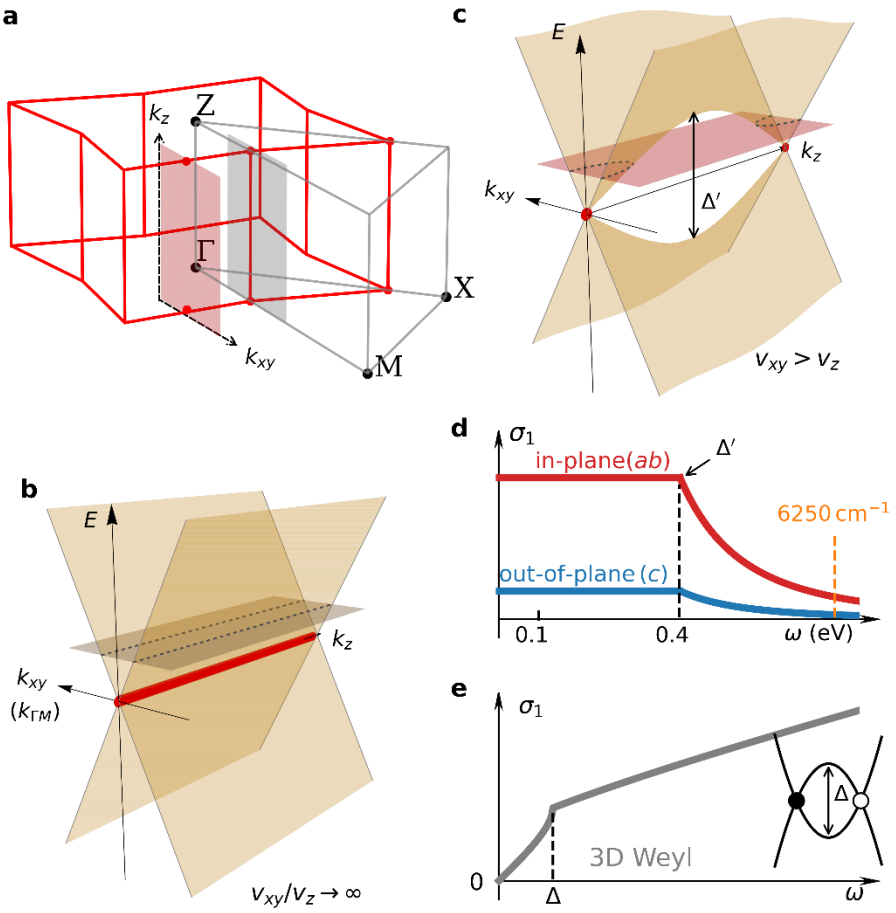

Figure S2. **a**. Schematic of cage-like nodal lines (red) in the Brillouin zone of ZrSiSe. **b**. Energy (E) versus momentum (k_{xy} and k_z) dispersion along a vertical nodal-line shown in panel **a** (grey-shaded region). For an energy flat nodal-line (red), the Fermi velocity along the line direction is zero ($v_z = 0$) while the Fermi velocity perpendicular to the lines (v_{xy}) remains large. **c**. E versus k_{xy} and k_z dispersion away from vertical nodal-lines (the red-shaded plane in **a**). Interband optical transitions are strongly suppressed above the Van Hove singularities (black arrow) at energy Δ'. **d**. Schematic of the real part $\sigma_1(\omega)$ of the optical conductivity of ZrSiSe, where the frequency-independent behavior terminates at $\Delta' \approx 0.4$ eV and reaches a local minimum around 0.77 eV ($\approx 6250\ cm^{-1}$). **e**. Schematic of $\sigma_1(\omega)$ for a pair of three-dimensional (3D) Weyl points also exhibiting Van Hove singularity (inset). Above the singularity energy, the linear increase of $\sigma_1(\omega)$ persists with a reduced slope.

Section S2: **Additional near-field imaging data and fitting**

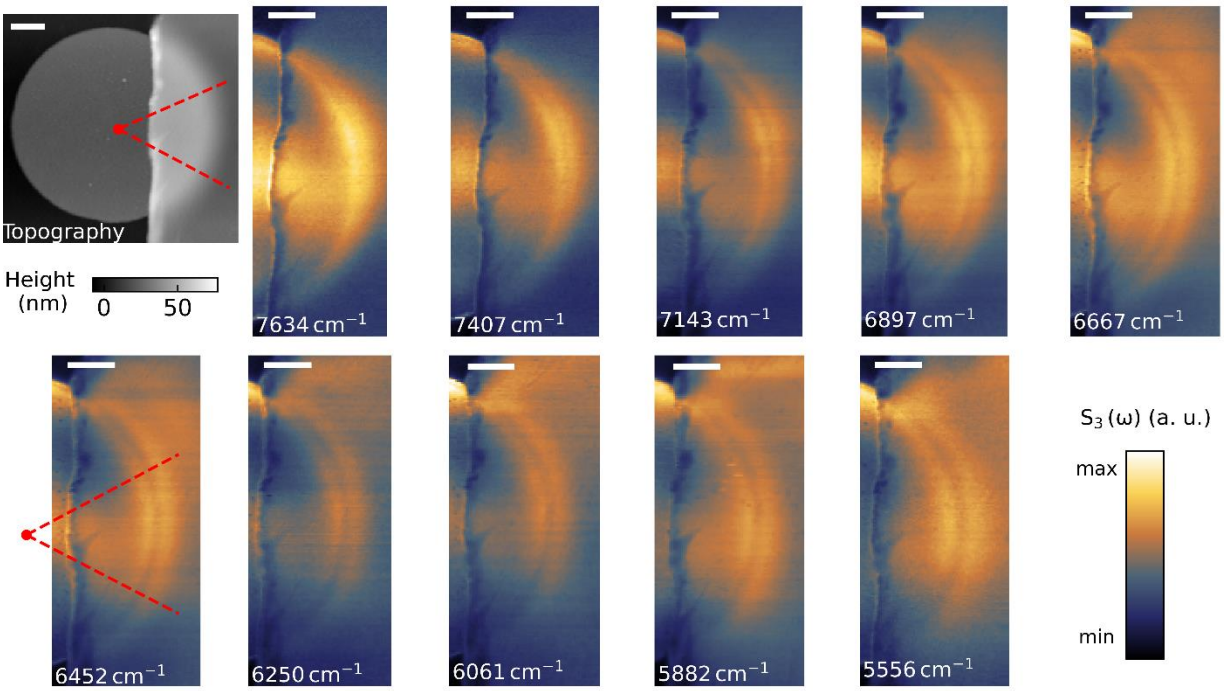

Figure S3. Topography and frequency-dependent near-field scattering amplitude data (S_3) of the 26 nm ZrSiSe sample (right) on a gold disk antenna. Scale bars in all panels are 300 nm. Red dashed lines indicate the sector region used to average the line profiles of S_3 along the perimeter of the disk antenna and are kept the same for all frequencies.

In Fig. S3 we show the full frequency dependence of the antenna launching experimental data in the hyperbolic regime. Since the diameter of the Au disk antenna (2 μm) is comparable to the laser wavelength ($1.3 - 1.8$ μm), the near-field signal exhibits diffraction patterns inside the Au antenna, as shown in the main text. On the other hand, the ZrSiSe region covering the Au antenna shows an enhancement in near-field amplitude and a gradual increase in the "double-ring" separation. This separation reaches a maximum at $\omega = 5556$ cm^{-1} and the length scale (≈190 nm) is an order of magnitude smaller than the laser wavelength ($\lambda = 1.8$ μm).

To quantify the double-ring separations, we fitted the line profiles of S_3 with Gaussian functions and a linear background, as shown in Fig. S4. Together with the slope correction discussed in the Methods section of the main text, we extracted the frequency-dependent peak separation $\delta(\omega)$, as shown in Fig. S5. The out-of-plane (*c*-axis) dielectric constant of ZrSiSe is then obtained using the experimental *ab*-plane dielectric constant and $\delta(\omega)$, according to $\sqrt{\varepsilon_c} = i\sqrt{\varepsilon_{ab}}(2d/\delta)$, where *d* is the thickness of the ZrSiSe crystal.

The extracted *c*-axis dielectric functions of ZrSiSe are modeled with Drude-Lorentzian oscillators accounting for both the intraband and the interband contributions: $\varepsilon_c(\omega) = \varepsilon_\infty +$

$\sum_j \frac{\omega_{p,j}^2}{\omega_{0,j}^2-\omega^2-i\gamma_j\omega}$. Here ε_∞ is the high-frequency dielectric constant, $\omega_{0,j}$, $\omega_{p,j}^2$ and γ_j are the center frequency, oscillator strength, and scattering rate of the j-th oscillator, respectively. The model (red line in Fig. S5) agrees well with the experimental data and the fitting parameters are listed in Table. S1.

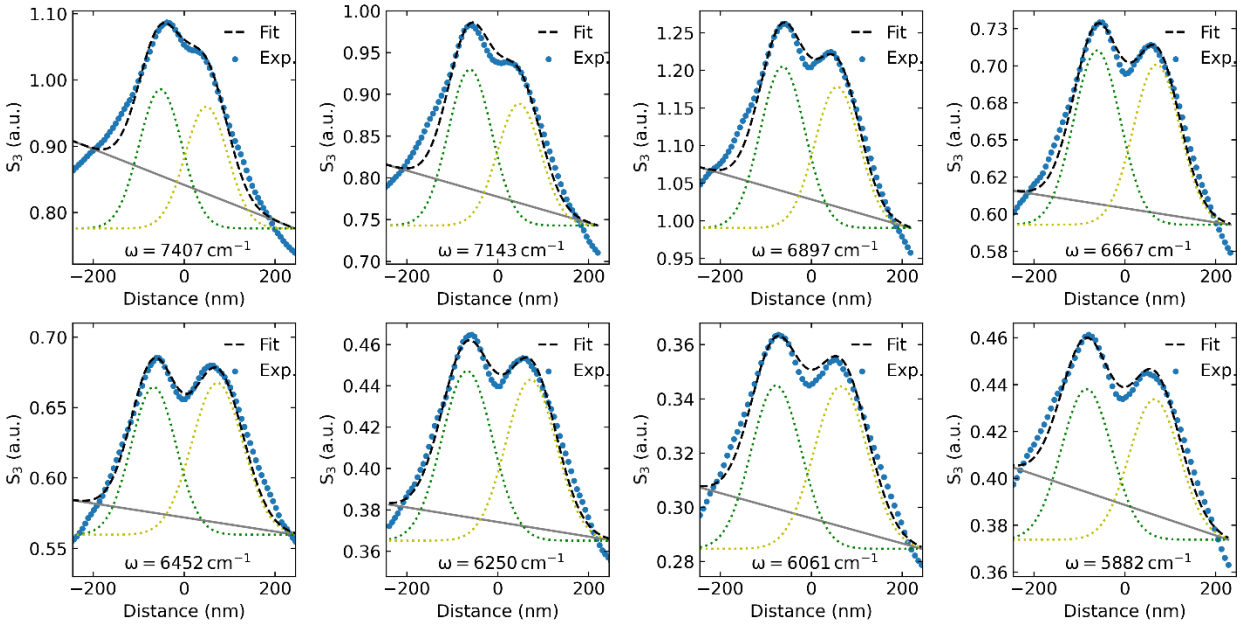

Figure S4. Frequency-dependent line profiles in the sample region from Fig.S3 are shown as blue dots. The extracted line profiles are fitted with two Gaussian profiles (green and yellow dotted lines) and linear backgrounds (gray solid lines). Black dashed lines are the sum of the Gaussians and the background, showing good agreement with the experiment.

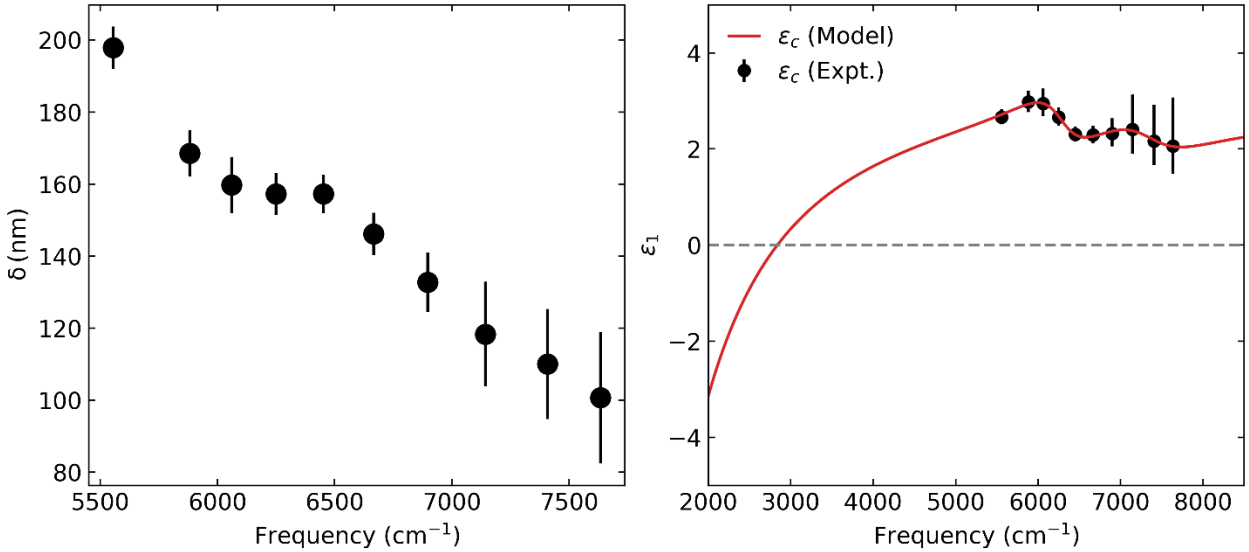

Figure S5. (Left) Experimental peak separation $\delta(\omega)$ obtained from the fitting in Fig. S4 and the slope correction discussed in the main text. (Right) Drude-Lorentz model fitting of the *c*-axis dielectric function data (black dots), obtained through the antenna launching experiment.

j	$\omega_{0,j}\ (cm^{-1})$	$\omega_{p,j}\ (cm^{-1})$	$\gamma_j\ (cm^{-1})$
1	0	5127.2	400.0
2	6291.3	2057.4	715.2
3	7367.8	2242.8	1055.3

Table S1. Parameters for the Drude-Lorentz model fitting of the experimental out-of-plane dielectric function of ZrSiSe using $\varepsilon_c(\omega) = \varepsilon_\infty + \sum_j \omega_{p,j}^2/(\omega_{0,j}^2 - \omega^2 - i\gamma_j\omega)$. Here, ε_∞=2.96 is the high frequency dielectric constant.

In Fig. S6 – Fig. S8, we show the gold disk antenna launching experiment with ZrSiSe crystals of varying thicknesses on top. Additional data with ZrSiSe crystals of thickness 25 nm and 40 nm are also shown as Extended Data Fig.3 and Extended Data Fig.4 in the main text, respectively.

In Fig. S9, we show the complete frequency-dependent near-field phase data (ϕ_4) for the 20 nm thin ZrSiSe crystal on the SiO_2/Si substrate. Dashed lines indicate the paths along which we extract the line profiles, shown in Fig. S10.

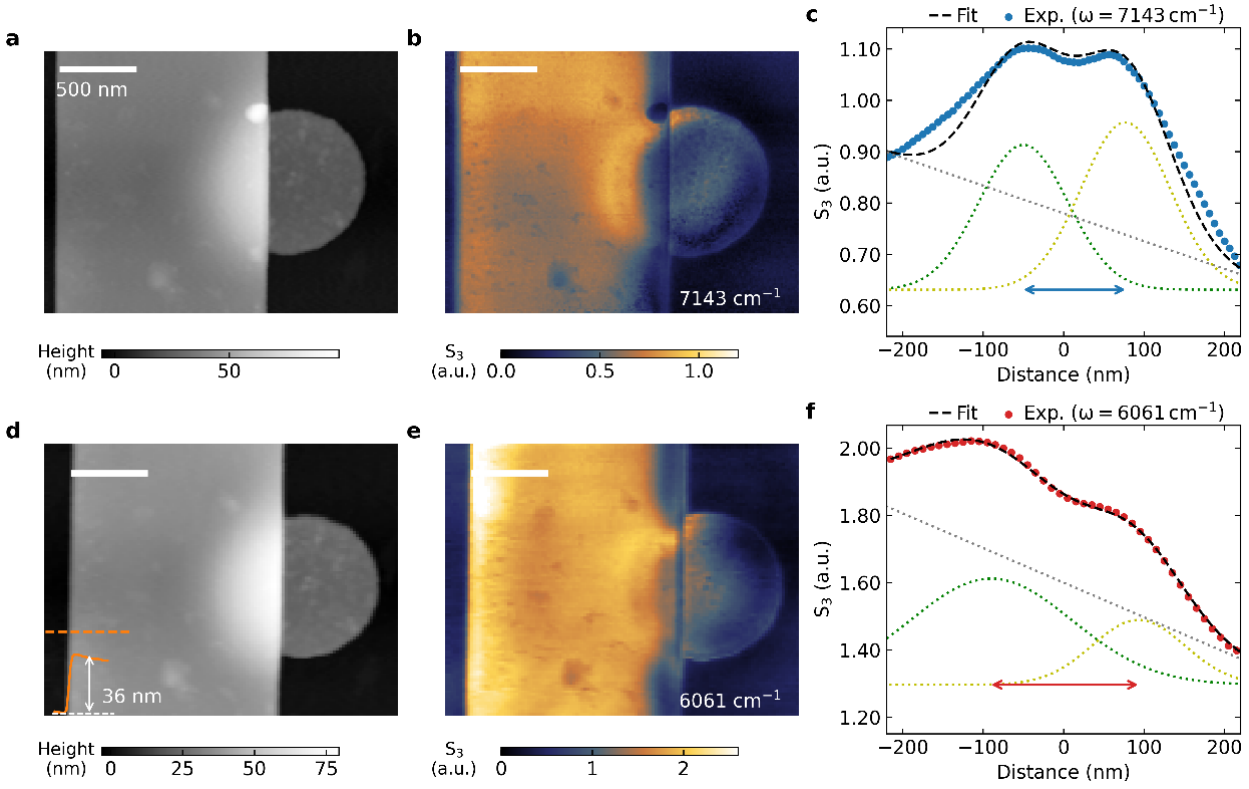

Figure S6. Topography and the corresponding near-field amplitude data (S_3) at (**a**, **b**) $\omega = 7143\ cm^{-1}$ and (**d**, **e**) $\omega = 6061\ cm^{-1}$ for the 36 nm thick ZrSiSe crystal on a Au antenna. Inset in panel **d** is the topography line profile along the orange dashed line. The extracted near-field amplitude line profiles on the sample along the perimeter of the antenna are shown for 7143 cm^{-1} and 6061 cm^{-1} in **c** and **f**, respectively. The line profiles are fitted with Gaussian functions (green and yellow dotted lines) and a linear background (grey dotted line). Scale bars in panels **a**-**d** are 500 nm.

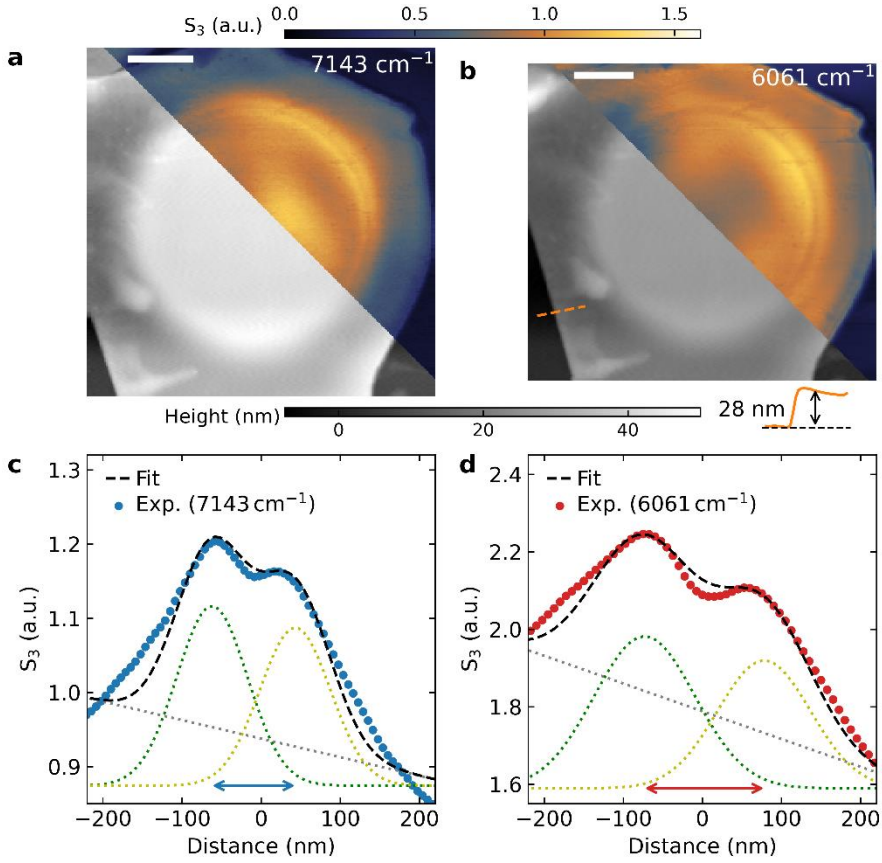

Figure S7. Topography (bottom) and the near-field amplitude data (top) at (**a**) $\omega = 7143\ cm^{-1}$ and (**b**) $\omega = 6061\ cm^{-1}$ for the 28 nm thick ZrSiSe crystal on a Au antenna. The extracted near-field amplitude line profiles on the sample along the perimeter of the antenna are shown for $7143\ cm^{-1}$ and $6061\ cm^{-1}$ in **c** and **d**, respectively. The line profiles are fitted with Gaussian functions (green and yellow dotted lines) and a linear background (grey dotted line). Scale bars in panels **a**,**b** are 500 nm.

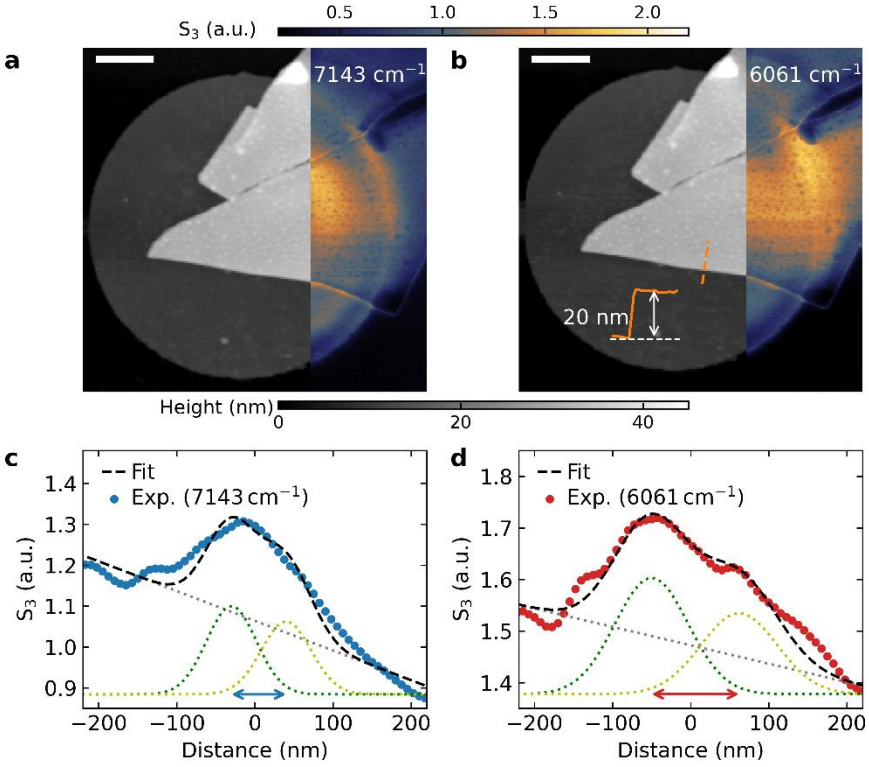

Figure S8. Topography (bottom) and the corresponding near-field amplitude data (top) at (**a**) $\omega = 7143\ cm^{-1}$ and (**b**) $\omega = 6061\ cm^{-1}$ for the 20 nm thick ZrSiSe crystal on a Au antenna. Inset in panel **b** is the topography line profile along the orange dashed line. The extracted near-field amplitude line profiles on the sample along the perimeter of the antenna are shown for $7143\ cm^{-1}$ and $6061\ cm^{-1}$ in **c** and **d**, respectively. The line profiles are fitted with Gaussian functions (green and yellow dotted lines) and a linear background (grey dotted line). Scale bars in **a**,**b** are 500 nm.

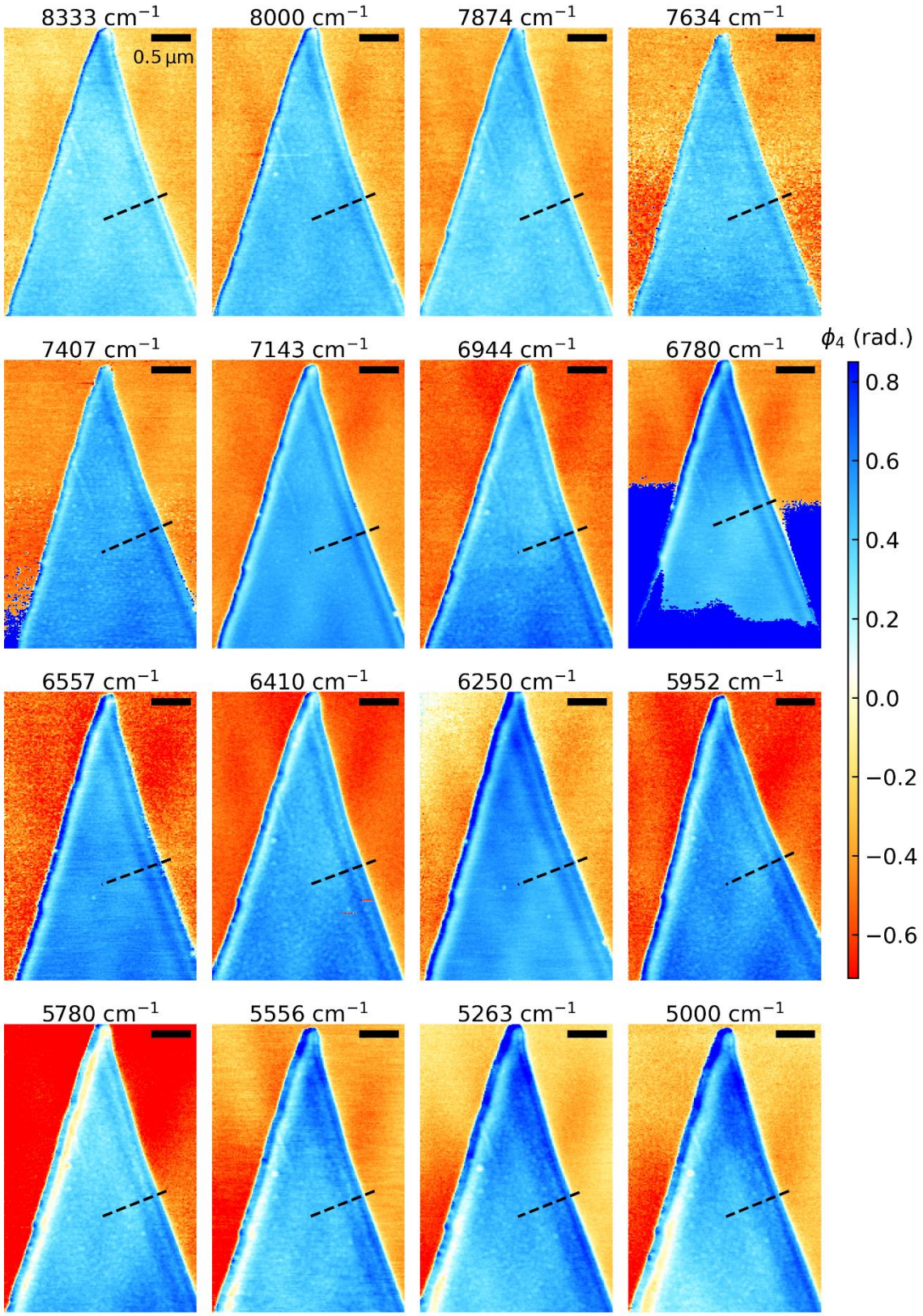

Figure S9. Frequency-dependent ($\omega = 8333 - 5000\ cm^{-1}$) near-field phase ($\phi_4$) for the 20 nm ZrSiSe on SiO_2/Si. Scale bars are 500 nm.

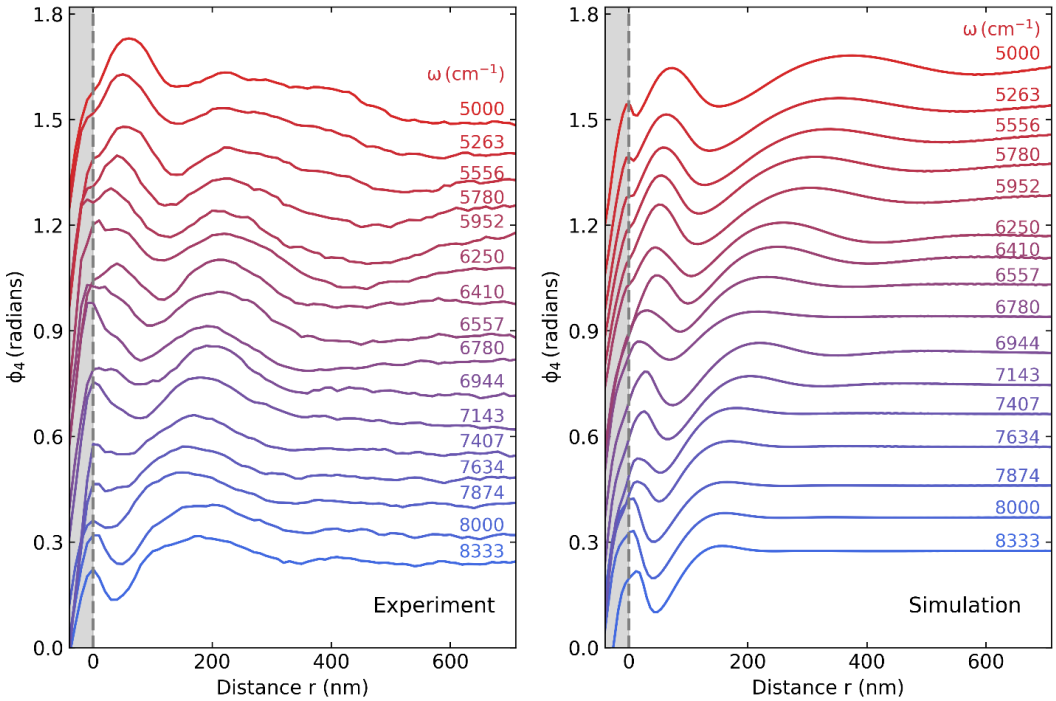

Figure S10. (Left) Line profiles of near-field phase (ϕ_4) along the black dashed lines in Fig. S9 for the 20 nm ZrSiSe on SiO_2/Si. (Right) Simulation of the phase line profiles at corresponding frequencies using the same parameters as for the simulation shown in the main text (Fig. 3).

Section S3: **Modeling the near-field signal near antenna edges**

To model the spatial profile of the signal near the edge of the gold disk, we develop an approximate solution for the scattered field created by a conducting disk, including the effects of diffraction. The basis of this approximation is Sommerfeld's solution to the famous problem of diffraction by a perfectly conducting screen[8]. Below, we review this solution and use it to construct an approximate solution for a metallic disk covered by a thin optically hyperbolic film.

Consider first a wave, incident at an angle α with respect to the plane with no component parallel to the edge of the conducting screen ($\beta = 0$), which we denote as the *y*-direction (Fig. S11 left). For concreteness, we first consider the case of a magnetic field $\boldsymbol{H} = H_y\hat{\boldsymbol{y}}$, where the scattered magnetic field has only one component along the *y*-direction, $H_y = U^{\perp}(x,z)$. The scattered magnetic field can be expressed through Fresnel diffraction integrals $F(z)$:

$$U^{\perp}(x,z;k) = U_0(x)\left(\frac{e^{ikz\sin\alpha+i\pi/4}}{\sqrt{\pi}}\left(F(\eta_+)+\frac{e^{-ikz\sin\alpha+i\pi/4}}{\sqrt{\pi}}F(\eta_-)\right)-isin(kz\sin\alpha)\right) \quad (1)$$

where $F(z) = \int_0^z e^{-i\kappa^2}d\kappa$, $\eta_{\pm} = \sqrt{2kr}\cos\frac{\phi\mp\alpha}{2}$, and $U_0(x) = E_0 e^{ikx\cos\alpha}$. Here k is the free-space photon wavevector, and (r, ϕ) represents polar coordinates in the xz-plane with $\tan\phi = z/x$ and $r = \sqrt{x^2+z^2}$. For the other, orthogonal polarization with the incident electric field $\boldsymbol{E} = E_y\hat{\boldsymbol{y}}$, one obtains the second solution for $E_y = U^{\parallel}(x,z)$:

$$U^{\parallel}(x,z;k) = U_0(x)\left(\frac{e^{ikz\sin\alpha+i\pi/4}}{\sqrt{\pi}}\left(F(\eta_+)-\frac{e^{-ikz\sin\alpha+i\pi/4}}{\sqrt{\pi}}F(\eta_-)\right)-cos(kz\sin\alpha)\right) \quad (2)$$

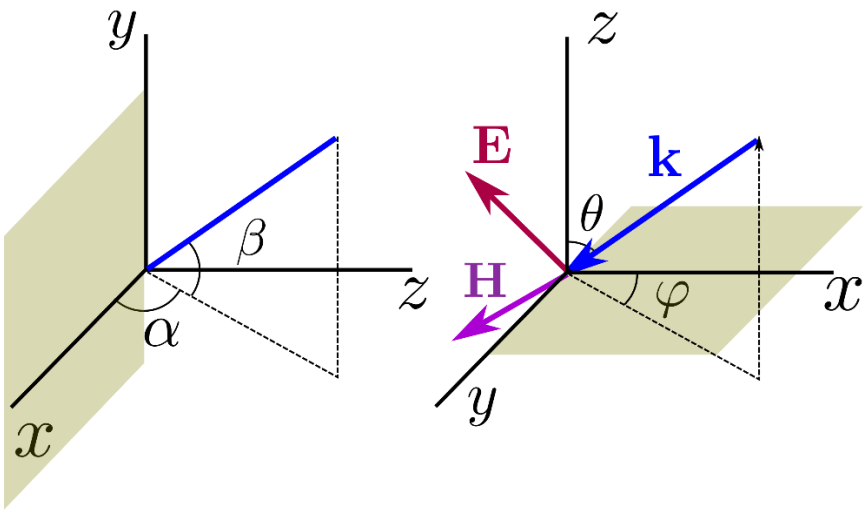

Figure S11. A schematic illustrating different choices of coordinate systems used in the expressions for the scattered fields. The shaded region represents the conducting screen creating the diffraction pattern, with the screen running parallel to the *y*-axis.

An arbitrary incidence angle relative to the edge can be accomplished by introducing an angle β, understood as a latitude relative to the *y*-axis, shown in Fig. S11. The angles α, β are related to the incidence angles θ, ϕ of a spherical polar coordinate system by the relations:

$$\cos\alpha\cos\beta = \cos\psi\sin\theta$$

$$\sin\beta = \sin\psi\sin\theta$$

$$\sin\alpha\cos\beta = \cos\theta$$

The z-component of the scattered electric field for an incident *p*-polarized light can then be decomposed into the polarizations of the fundamental solutions $U^{\perp}, U^{\parallel}$[14], yielding:

$$E_z^{sca}(x,y,z;k) = e^{ikysin\beta}\left[A\frac{i}{k}\frac{\partial}{\partial x}\left(U^{\perp}(x,z;k\cos\beta)\right) + B\frac{i\sin\beta}{k}\frac{\partial}{\partial z}\left(U^{\parallel}(x,z;k\cos\beta)\right)\right] \quad (3)$$

The coefficients A, B arise from the decomposition of the polarization of the incident wave into components parallel and perpendicular to the edge of the screen and depend only on the polar and in-plane incidence angles α, β. We can then construct an approximate solution for a disk by solving for several angles ψ and plotting the diffraction pattern produced for each angle, with the out-of-plane component E_z plotted in Fig. S12a at a frequency of $\omega = 6600\ cm^{-1}$.

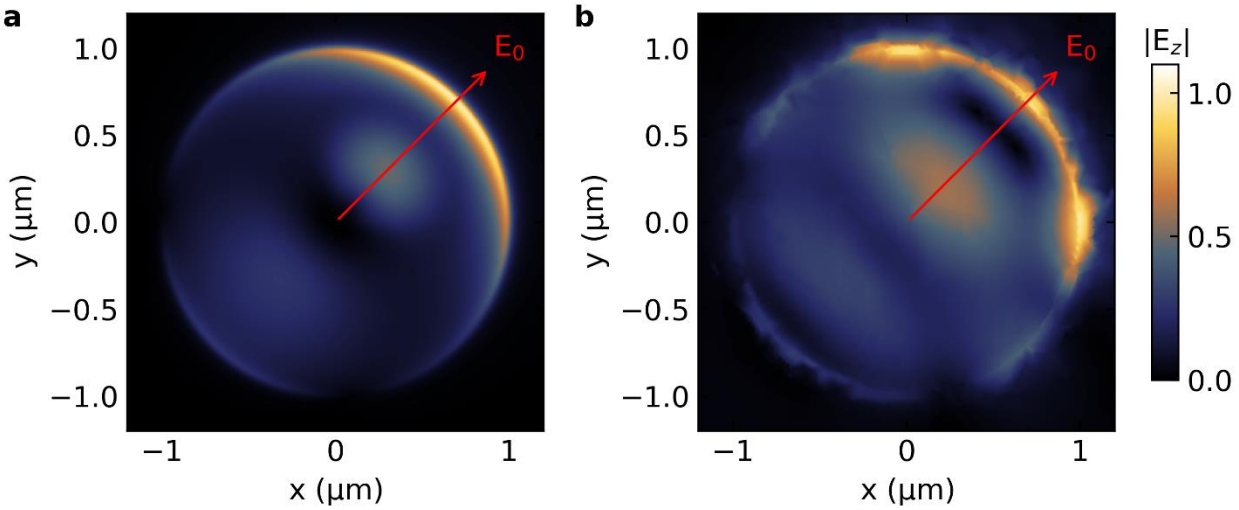

Figure S12. Absolute value of the z-component of the scattered field E_z at a height of 25 nm above the disk, obtained using the approximate model (**a)** and the numerical solution (**b)**. The direction of the incident field is highlighted by the red arrow in both panels.

To check the validity of this approximation, we used the COMSOL package to simulate the scattered field distribution produced by a plane wave whose magnetic field was polarized parallel to the disk. This numerical approach was necessitated by the large free-space wavelength, which is comparable to the size of the metallic disk, invalidating the quasistatic approximation typically used in the modeling of the SNOM signal. The disk was included by implementing a perfectly conducting boundary condition on the surface of the disk inside of a physical domain of dimension $4\ \mu m \times 4\ \mu m \times 2\ \mu m$ padded with perfectly matched layers of

thickness 500 nm at each edge of the domain. A scattering boundary condition was implemented at the edge of the physical domain, and only the scattered field was extracted. The result of this simulation is plotted in Fig. S12b. The agreement between the approximation and the numerical solution is expected to hold only near the edge of the disk, which contains the crucial feature, namely a divergence of the field due to a sharp edge. The angular intensity distribution around the circumference of the disk is also captured by the approximate model, which can then be modified to account for the effect of the hyperbolic medium.

The introduction of the sample will bring with it the hyperbolic modes and modify the scattered field. The multiple branches of the polariton dispersion observed are derived by computing the poles in the reflection coefficient $r_p(q,\omega)$ in the absence of losses. In a realistic system with finite loss, the dispersion is instead dictated by the maxima in Im $r_p(q,\omega)$. We consider a three-layer system consisting of vacuum, sample and substrate, labeled as medium 0, 1 and 2, respectively. The divergence of $r_p(q,\omega)$ happens at a discrete set of values satisfying the condition:

$$2\pi l + \psi_{01} + \psi_{21} = 2k_1^z d \tag{4}$$

for a medium of thickness *d*. The phase shifts ψ_{01}, ψ_{21} can be expressed in terms of reflection coefficients at the top and bottom interfaces, $r_{01} = e^{i\psi_{01}}$ and $r_{21} = e^{i\psi_{21}}$, respectively. The reflection coefficients r_{ij} at the interfaces are given by:

$$r_{ij}(q) = \frac{\varepsilon_j^{\perp}/k_j^z - \varepsilon_i^{\perp}/k_i^z}{\varepsilon_j^{\perp}/k_j^z + \varepsilon_i^{\perp}/k_i^z} \tag{5}$$

where the *z*-component of the wavevector k_i^z of a *p*-polarized light in each medium is given by:

$$k_i^z(q) = \sqrt{\varepsilon_i^{\perp}}\sqrt{\frac{\omega^2}{c^2} - \frac{q^2}{\varepsilon_i^z}}, \qquad \text{Im } k_i^z > 0 \tag{6}$$

In the hyperbolic regime ($q \gg \omega/c$), k_1^z is predominantly real, so the solutions of Eqn. (4) are not confined to a surface but can exist within the bulk of the sample. A closed-form solution for the dispersion can only be obtained within the quasistatic approximation ($c \to \infty$). In that case, the reflection coefficients of Eqn. (5) become independent of q and reduce to:

$$\beta_{ij} = \frac{\sqrt{\varepsilon_j^{\perp}}\sqrt{\varepsilon_j^z} - \sqrt{\varepsilon_i^{\perp}}\sqrt{\varepsilon_i^z}}{\sqrt{\varepsilon_j^{\perp}}\sqrt{\varepsilon_j^z} + \sqrt{\varepsilon_i^{\perp}}\sqrt{\varepsilon_i^z}} \tag{7}$$

The original transcendental equation Eqn. (4) reduces to a linear equation for the dispersion of each mode q_l. In the particular case of launching by a conducting metallic edge, the observed fringes in real space can be understood as a beating between the various modes q_l in momentum space[9], giving a fringe spacing of:

$$\lambda_p = \frac{2\pi}{\Delta q_l} \approx -2id\frac{\sqrt{\varepsilon_1^{\perp}}}{\sqrt{\varepsilon_1^{z}}} \tag{8}$$

with the last equality holding in the quasistatic limit.

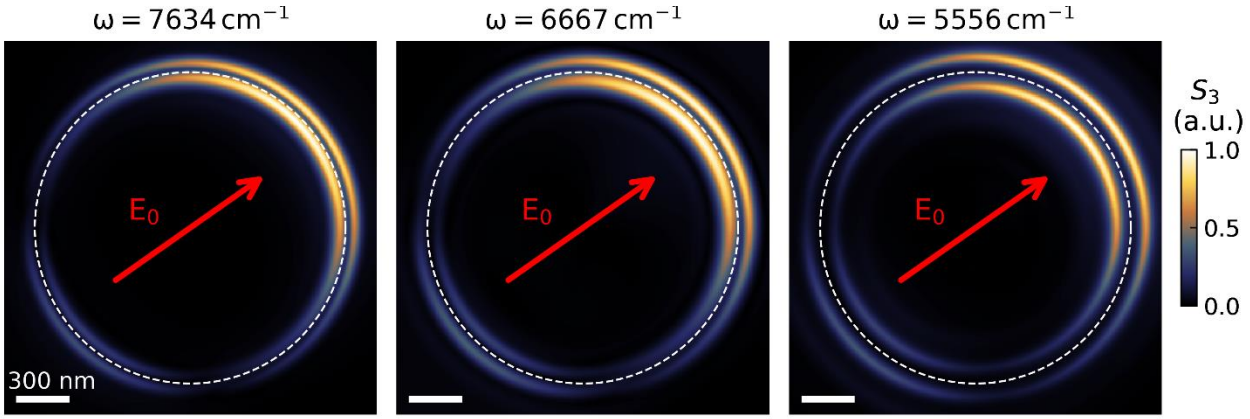

Figure S13. Simulated near-field amplitude of ZrSiSe (26.5 nm) on a gold disk (25 nm) obtained from the approximate model at $\omega = 7634\ cm^{-1}, 6667\ cm^{-1}, 5556\ cm^{-1}$. The edge of the gold disk is shown by the white dashed line and the direction of the field is indicated by the red arrow.

Having previously obtained a solution for the field created in vacuum by a screen, this expression can be used as a building block to construct an approximate solution to the field produced by the system of the disk, sample, and substrate. Since the polariton wavelength (λ_p) is an order of magnitude smaller than the free-space photon wavelength λ_0, near the edge we expect a quasistatic approximation to be valid, permitting the use of an image method to introduce a sample[9]. Using the field from Eqn. (3), we introduce an equidistant series of images, as in the solution for the static field of a dielectric film between two media. We take the infinitely thin disk as the source of this static field, situated at the interface of media 1 and 2, that is, below the ZrSiSe layer. For an optically anisotropic material, the thickness of the film is further modified by the ratio of in-plane and z-axis dielectric function: $\sqrt{\varepsilon^t}/\sqrt{\varepsilon^z}$. The scattered near-field signal (S) can be approximated as the z-components of the field E_z^s obtained from the diffraction problem and the reflection coefficients β_{ij} from Eqn. (7):

$$S(x,y,z) = (1-\beta_{01})E_z^{sca}(x,y,z+h) + \beta_{21}(1+\beta_{01})\sum_{n=1}^{\infty}\beta_{01}^n\beta_{21}^n E_z^{sca}\left(x,y,(2n+1)d\frac{\sqrt{\varepsilon^t}}{\sqrt{\varepsilon^z}}+h\right) \tag{9}$$

To include the effects of demodulation, we compute the field at a discrete set of points above the sample:

$$h(t) = h_0 + \Delta h(1-\cos n\Omega t) \tag{10}$$

to obtain the complex signal $\tilde{s_n} = S_n e^{i\phi_n}$. Here Ω is the tip-tapping frequency and we used tapping amplitude $\Delta h = 50\ nm$ and minimum position $h_0 = 5\ nm$. The demodulated scattering amplitudes ($n = 3$) computed as a few different frequencies are shown in Fig. S13.

Section S4: Electronic structure calculations of ZrSiSe

The electronic structure of the system was investigated with density functional theory (DFT). DFT calculations were carried out at the level of DFT plus onsite Hubbard U and intersite V (DFT+U+V)[10], as implemented in the Octopus code[11], which delivers an hybrid-like quality of the band structure at a fraction of the computational cost[12]. Experimental lattice constants of $a = 3.623$ Å and $c = 8.365$ Å were employed. For the slab configuration, containing 5 layers of ZrSiSe, a 16 Å vacuum region was chosen to properly converge the bands along the non-periodic dimension z. The ground state was calculated by discretizing the equations in real-space with a spacing of 0.159 Å and spin-orbit coupling was fully accounted for valence electrons while core electrons were treated with relativistic HGH pseudopotentials[13]. The Brillouin zone was sampled with a 16×16×8 Monkhorst-Pack grid for the bulk and a 15×15 grid for the slab geometries.

References

1. Shao, Y. *et al.* Electronic correlations in nodal-line semimetals. *Nat. Phys.* **16**, 636–641 (2020).
2. Ebad-Allah, J. *et al.* Pressure-Induced Excitations in the Out-of-Plane Optical Response of the Nodal-Line Semimetal ZrSiS. *Phys. Rev. Lett.* **127**, 076402 (2021).
3. Schilling, M. B., Schoop, L. M., Lotsch, B. V., Dressel, M. & Pronin, A. V. Flat Optical Conductivity in ZrSiS due to Two-Dimensional Dirac Bands. *Phys. Rev. Lett.* **119**, 187401 (2017).
4. Shao, Y. *et al.* Optical signatures of Dirac nodal lines in NbAs2. *PNAS* **116**, 1168–1173 (2019).
5. Habe, T. & Koshino, M. Dynamical conductivity in the topological nodal-line semimetal ZrSiS. *Phys. Rev. B* **98**, 125201 (2018).
6. Xu, B. *et al.* Optical spectroscopy of the Weyl semimetal TaAs. *Phys. Rev. B* **93**, 121110 (2016).
7. Tabert, C. J. & Carbotte, J. P. Optical conductivity of Weyl semimetals and signatures of the gapped semimetal phase transition. *Phys. Rev. B* **93**, 085442 (2016).
8. Sommerfeld, A., Laporte, O. & Moldauer, P. A. Optics: Vol. 5 of Lectures on Theoretical Physics. *Physics Today* **8**, 16–16 (1955).
9. Dai, S. *et al.* Subdiffractional focusing and guiding of polaritonic rays in a natural hyperbolic material. *Nat. Commun.* **6**, 6963 (2015).
10. Tancogne-Dejean, N. & Rubio, A. Parameter-free hybridlike functional based on an extended Hubbard model: $\mathrm{DFT}+U+V$. *Phys. Rev. B* **102**, 155117 (2020).
11. Tancogne-Dejean, N. *et al.* Octopus, a computational framework for exploring light-driven phenomena and quantum dynamics in extended and finite systems. *J. Chem. Phys.* **152**, 124119 (2020).
12. Gatti, G. *et al.* Light-Induced Renormalization of the Dirac Quasiparticles in the Nodal-Line Semimetal ZrSiSe. *Phys. Rev. Lett.* **125**, 076401 (2020).
13. Hartwigsen, C., Goedecker, S. & Hutter, J. Relativistic separable dual-space Gaussian pseudopotentials from H to Rn. *Phys. Rev. B* **58**, 3641–3662 (1998).